JOURNAL OF PROPULSION AND POWER
Vol. 15, No. 4, July–August 1999

Numerical Study of Cavitation in the Wake of a Hypervelocity Underwater Projectile

Richard Saurel* and Jean Pierre Cocchi†
Institut Universitaire des Systemes Thermiques Industriels, 13453 Marseille CEDEX 13, France
and
P. Barry Butler‡
University of Iowa, Iowa City, Iowa 52242

The focus of this study is on cavitation in the wake of a high-velocity underwater projectile. A physical model based on the Euler equations is presented in terms of two-phase mixture properties. Mathematical closure is achieved by providing equations of state for the possible thermodynamic states: compressible liquid, compressible two-phase mixture, and compressible pure vapor. For the operating conditions studied here, all states are subcritical. The proposed model is solved using a hybrid computational scheme developed to accurately resolve property profiles across discontinuities. The model is validated with several one-dimensional test cases that have known analytic solutions. For modeling the hypervelocity underwater projectile, the model is shown to compute unsteady shock-wave development as well as the projectile-wake cavitation zone. The model is then used to conduct a parametric study on the affect of flow and projectile properties on cavitation.

Nomenclature

a_i, b_i, c_i	= coefficients of the Oldenbourg polynomials
C_v	= specific heat at constant volume
E	= specific total energy
e	= specific internal energy
$\boldsymbol{F}, \boldsymbol{G}$	= vector of conservative fluxes
$\boldsymbol{H}$	= vector of axisymmetric terms
K_0	= bulk modulus in the Tait equation of state
L_v	= latent heat of vaporization
n	= density exponent in the Tait equation of state
P	= pressure
R	= gas constant per unit mass
r	= radial coordinate
s	= specific entropy
T	= temperature
t	= time
$\boldsymbol{U}$	= vector of conservative variables
u	= z-velocity component
$\boldsymbol{u}$	= velocity vector
V	= volume
v	= r-velocity component
x	= space coordinate
z	= longitudinal coordinate
α	= volume fraction
ρ	= density

Subscripts

c	= properties at the critical point
g	= gas
l	= liquid
sat	= saturation properties

Received 13 November 1997; revision received 20 November 1998; accepted for publication 30 November 1998.

*Professor, Unite Mixte de Recherche du Centre National de la Recherche Scientifique, 6595, 5 rue Enrico Fermi.
†Ph.D. Student, Unite Mixte de Recherche du Centre National de la Recherche Scientifique, 6595, 5 rue Enrico Fermi.
‡Professor, Department of Mechanical Engineering, 2408 Engineering Building.

I. Introduction

MOST theoretical and numerical studies of cavitation consider the liquid component to be at a low Mach number and be incompressible.[1–3] However, when dealing with very-high-velocity flows (several kilometers per second) over a rigid projectile, liquid compressibility, and phase change caused by low pressure, post-shock expansion regions must also be addressed. The published literature is limited on this subject.[4] This type of high-velocity, compressible flow in water can be achieved with detonation-driven projectiles.[5] Similar flow processes leading to cavitation can also occur when high-pressure liquid fuel is injected at high velocity into engine combustion chambers. Some high-pressure-injection devices yield fuel velocities of several hundred meters per second. At the nozzle inlet throat of such a device, the pressure drop is such that cavitation effects are predominant. This has serious consequences on the dynamics of jet atomization.[6]

The present research focuses on cavitation effects in the wake of a high-velocity projectile in water. For this unique flow configuration it is important to understand and quantify the shape and thermodynamic behavior of the wake formed in the low-pressure region behind the projectile because it couples directly with its performance. Cavitation resulting from high-velocity flow over a projectile poses many interesting problems such as multidimensional liquid-phase compressive shocks, liquid–vapor phase change, and rarefaction waves in both liquid and gaseous components. In addition, knowledge of the vapor pocket size and internal density profile is very important if another projectile is expected to propagate in the wake of the primary projectile. In practice, it is possible for a secondary projectile to benefit from the wake effects of a primary, explosively driven projectile. This is particularly important when the kinetic energy of the secondary projectile is used for impact and penetration into solid targets.

The main objective of the present work is to develop and validate a model for studying the flow around a high-velocity underwater projectile. A specific goal is to predict the cavitation envelope's shape as a function of boundary and flow conditions. The model and proposed solution methodology will be validated for a one-dimensional problem that has a known analytic solution. Following the validation exercise, the model will be extended to the more complex two-dimensional hypervelocity projectile and predictions of the wake structure will be performed.

An underwater projectile moving at high velocity is illustrated in Fig. 1. The projectile has conical-shaped leading and trailing edges

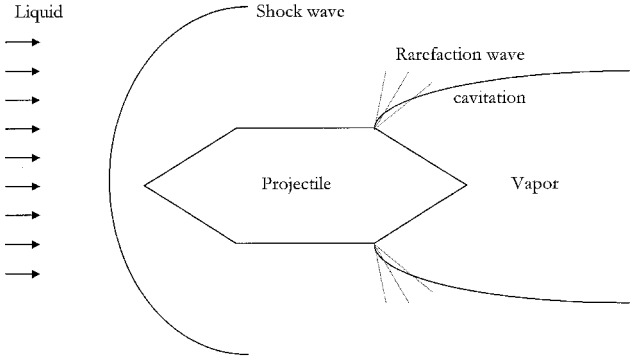

Fig. 1 Illustration of flow around hypersonic underwater projectile.

and a cylindrical centerbody. It is propagating through liquid water that is at standard-state conditions ahead of the projectile. The projectile velocity is supersonic with respect to the liquid sound speed (>1600 m/s). Thus, a shock wave is either present in front of the body (bowshock as shown in the figure), or attached to the leading edge at an oblique angle relative to the oncoming flow. Geometrical effects then induce additional compression and rarefaction waves as the flow progresses over the body and encounters changes in the surface flow direction. Under certain conditions the expansion wave produced by the geometry of the projectile trailing edge can result in liquid vaporization in the wake of the projectile. For simplification, the projectile will be assumed herein to be of constant shape and size; i.e., surface erosion is not considered. The primary interest of this study is on the flow features around, and in the near wake of the projectile. This defines length and time scales during which erosion is not a dominant phenomena.

Depending on the local pressure and temperature of the fluid, a wide range of thermodynamic states are possible in the compression and expansion regions surrounding the projectile. For example, when the incident flow velocity is very high, the liquid compressibility is important and strong shock waves (>50 kbar) may be present. On the other hand, gas-phase states are expected in the wake of the projectile as a result of excessively low pressures (subatmospheric). Between these two extreme pressure limits, partial vaporization states are possible. This results in a two-phase mixture where both liquid and gas are compressible.

In the following section, several possible approaches to model the problem at hand are introduced. Following this is a discussion of the proposed model that is based on the assumptions of an inviscid compressible flow model and phase equilibrium between the gas and liquid. To complete the physical model it is necessary to develop an equation of state that covers all fluid states possible: compressible pure liquid, compressible two-phase mixture, and compressible pure gas (vapor). Accuracy of the resulting equation of state (EOS) is demonstrated by comparing its predictions with standard compressibility data for the respective phases. Following this, modifications to the numerical scheme to deal with flows exhibiting high velocities and low densities are discussed. In the results, a one-dimensional problem with known analytic solution is modeled to show the capabilities of the proposed model. The model is then applied to the two-dimensional hypervelocity projectile under flow conditions where cavitation is present.

II. Flow Model

It is first necessary to develop a physical model of multiphase hypervelocity flow, where both phases are compressible and the fluid states can range from pure liquid to pure gas throughout the flow domain. Several different approaches are possible and the relative merit of each will be discussed before presenting the form of the conservation equations selected for the present study.

One possible approach to modeling hypervelocity cavitation is based on the two-phase formulation of the conservation equations. Models where both phases are compressible are available in the literature, such as the so-called six- and seven-equation models.[7,8] However, these models were developed for very different flow conditions than those considered here. In fact, when dealing with hypervelocity cavitation, these models present some major drawbacks. First, the two-phase flow equations are not valid in the limit of pure liquid or pure gas flows. Second, these models are not able to reproduce the dynamics of an interface between two distinct phases of a fluid. In fact, these two-phase formulations of the conservation equations are not accurate when dealing with discontinuities in volume fraction. Evidence of this numerical difficuly has been pointed out by Rogue et al.[9] These formulations of the conservation equations are not mathematically closed at the interface, corresponding to a moving boundary for each subsystem of equations. Another reason is that nonconservative terms in the conservation equations pose many problems for numerical solutions. Consequently, numerical diffusion from any method produces an artificial two-phase zone where the pressure cannot be calculated correctly. The last drawback with applying the two-phase flow equations to hypervelocity cavitation is related to correctly modeling interphase mass transfer caused by a pressure drop. To date, no finite rate mass transfer model is available for the pressure range and the time scales studied herein.

An alternative method to model cavitation in the wake of a high-velocity projectile is to use the mixture approach. Here, the single-phase flow equations are solved with an appropriate EOS to account for the fluid's mixture state. The difficulty with this approach is that one must specify an EOS that covers all possible fluid states: pure liquid, two-phase mixture, and pure gas. In the next section, an EOS satisfying these constraints will be developed.

The flow model developed in this section is based on a single-phase representation of the Euler equations. For the present problem involving high-velocity flows in dense media, the pressure levels are typically very high (≫10 kbar). Under these conditions, the diagonal part of the stress tensor is dominant, and the deviatoric part, containing viscous and dissipative terms, becomes negligible. Consequently, the use of the Euler form of the equations is valid for predicting the qualitative shape of the cavitation envelope. It should be noted that the wake flowfield is strongly affected by the location of boundary-layer separation on the afterbody, and in the boundary layer the diagonal part of the stress tensor, i.e., pressure terms, are of the same order as some of the viscous terms. Thus, details of the wake structure cannot be accurately modeled without resorting to a viscous, i.e., Navier–Stokes, solution. It should also be emphasized that special consideration must be given to evaluating the fluid state during phase change when the flow is two phase. In the wake of the projectile, the pressure drops to subatmospheric levels.

Our flow model for the two-phase mixture induced by cavitation effects is based on the assumption of local thermodynamic equilibrium between phases. It specifies local temperature and pressure equality between phases. It also assumes that the gas and liquid components of the two-phase mixture have local velocity equilibrium. Based on these equilibrium constraints, the density and specific internal energy of the mixture can be expressed as the volume-weighted sum of the respective phases. Under these assumptions, the fundamental equations are the well-known Euler equations, written here in conservative form with mixture variables:

$$\frac{\partial \rho}{\partial t} + \nabla \cdot (\rho \boldsymbol{u}) = 0, \qquad \frac{\partial \rho \boldsymbol{u}}{\partial t} + \nabla (\rho \boldsymbol{u} \otimes \boldsymbol{u} + P) = 0$$
$$\frac{\partial \rho E}{\partial t} + \nabla \cdot [\boldsymbol{u}(\rho E + P)] = 0 \tag{1}$$

with

$$\rho = \alpha_g \rho_g + \alpha_l \rho_l, \qquad E = e + \tfrac{1}{2}\boldsymbol{u} \cdot \boldsymbol{u}$$
$$e = \alpha_g e_g + \alpha_l e_l, \qquad 1 = \alpha_g + \alpha_l \tag{2}$$

Here, subscript g refers to the gaseous (or vapor) phase, subscript l refers to the liquid phase, and mixture variables are written without any subscripts. For closure, it is necessary to develop an EOS that works for pure liquid, pure gas, and a gas–liquid mixture.

III. Equation of State

Previous studies have considered the liquid to be governed by the so-called stiffened gas EOS.[4] This type of model assumes that during fast time scales, e.g., characteristic of these studies, mass transfer cannot occur. Thus, the fluid remains a pure liquid, and the stiffened gas EOS has been used to model the full range of liquid density. For shock-compressed liquid states characteristic of hypervelocity underwater projectile, this EOS is reasonably accurate. However, for densities lower than ambient, this EOS is no longer valid. In fact, for the present application, the liquid density is expected to decrease by three orders of magnitude in going from the compressed states behind the leading shock front to the expanded flow states present in the wake of the projectile. When the stiffened gas EOS is used with densities lower than ambient, the predicted pressure is not reasonable.

More realistic EOSs that cover the range of densities of interest are available. For example, the Van der Walls EOS,[10] or the more sophisticated EOS proposed by Saul and Wagner[11] with 58 coefficients, have been tested. However, when dealing with phase transition, these EOSs are not compatible with the governing fluid dynamic equations. The Euler equations require a convex EOS.[12,13] By definition, the EOS is convex if the Hessian matrix, composed of the second derivatives of the EOS is positive definite:

$$\frac{\partial^2 e}{\partial \rho^2} > 0, \qquad \frac{\partial^2 e}{\partial s^2} > 0, \qquad \frac{\partial^2 e}{\partial \rho^2}\frac{\partial^2 e}{\partial s^2} - \left(\frac{\partial^2 e}{\partial \rho \partial s}\right)^2 > 0$$

The previously mentioned EOSs are not convex and cannot be used with the gasdynamic equations (except for flows with limited density variations). These EOSs present at least two points in the saturation zone where the second derivatives change signs, i.e., spinodal points.

The previous considerations have driven the need to construct a new EOS based on the assumption of local phase equilibrium during phase change. For each pure fluid phase, an appropriate EOS is selected and validated over a wide range of states. These pure-fluid EOSs are then linked together to yield a more general EOS that can accurately cover the entire range of possible fluid states. It should be emphasized that the resulting EOS is not valid for supercritical fluids. For the present applications, however, pressure and temperature conditions are such that supercritical fluid states are not expected. This statement will be validated later.

A. Liquid Phase EOS

An established EOS for modeling liquid water as a compressible fluid is the so-called Tait EOS.[14] This EOS was developed for modeling the response of liquid water to underwater explosions, and is given as

$$P = K_0\left[(\rho/\rho_0)^n - 1\right] + P_0 \tag{3}$$

where P_0 and ρ_0 are pressure and density at standard-state temperature, respectively. Parameters K_0 and n are weak functions of temperature and pressure. Here, they are assumed constant: $n = 7$ and $K_0 = 3 \times 10^8$ Pa (for water). Modifications are proposed to adapt Eq. (3) to treat the saturated liquid component of a two-phase mixture. To achieve this the reference properties are changed from P_0 and ρ_0 to the temperature-dependent saturation pressure $P_{\text{sat}}(T)$ and the corresponding liquid saturation density $\rho_{l\,\text{sat}}(T)$, respectively. With these changes, Eq. (3) represents a family of self-similar curves in the (P, ρ) plane, having their origin on the liquid-vapor saturation curve. With the change in reference states, Eq. (3) becomes

$$P = K_0\left\{\left[\frac{\rho}{\rho_{l\,\text{sat}}(T)}\right]^n - 1\right\} + P_{\text{sat}}(T) \tag{4}$$

The caloric EOS that is thermodynamically consistent with Eq. (3) is a constant specific heat relation:

$$e_l(T) = C_{vl}(T - T_0) + e_{l0} \tag{5}$$

where C_{vl} is the specific heat at constant volume (4.18 kJ/kg K for water), T_0 is the reference temperature (273.15 K), and e_{l0} is the reference energy at this temperature (0. 617 kJ/kg).

B. Gas-Phase EOS

For water in its vapor phase, the ideal gas EOS is used:

$$P = \rho R T \tag{6}$$

where $R = \hat{R}/\hat{M}$ represents the gas constant ($\hat{R}$ is the universal constant and $\hat{M}$ the molar mass). The corresponding gas-phase caloric EOS is

$$e_g(T) = Cv_g(T - T_0) + Lv(T_0) + e_{l0} \tag{7}$$

where Lv represents the latent heat of vaporization.

C. Saturation EOS

Two-phase mixtures defined by a unique (P, T) state in the saturation region are assumed to be in equilibrium: $P_l = P_g = P$ and $T_l = T_g = T$, where the pressure equals the saturation pressure $P = P_{\text{sat}}(T)$, and the temperature is equal to the saturation temperature: $T = T_{\text{sat}}$. The relation between pressure and temperature during phase change is given in a convenient form in Ref. 15:

$$\ln(P_{\text{sat}}/P_0) = (T_c/T_{\text{sat}})\left(a_1\theta + a_2\theta^{1.5} + a_3\theta^3 + a_4\theta^{3.5} + a_5\theta^4 + a_6\theta^{7.5}\right) \tag{8}$$

Equation (8) is the barotropic EOS, where $\theta = 1 - T/T_c$ and P_c and T_c represent the critical pressure and temperature, respectively. The critical conditions for water are $P_c = 22.64 \times 10^5$ Pa, $T_c = 647.14$ K, and $\rho_c = 332\,\text{kg/m}^3$. The other parameters for Eq. (8) are given in Table 1.

For the two-phase states, the temperature is determined from the definition of the internal energy of the mixture:

$$e(T) = \{[\alpha_g\rho_{g\,\text{sat}}(T)Cv_g + \alpha_l\rho_{l\,\text{sat}}(T)Cv_l](T - T_0) + \alpha_g\rho_{g\,\text{sat}}(T)Lv(T_0)\}/\rho + e_{l0} \tag{9}$$

The liquid and gas densities along the saturation curve are also given in Ref. 15:

$$\frac{\rho_{l\,\text{sat}}(T)}{\rho_c} = 1 + b_1\theta^{\frac{1}{3}} + b_2\theta^{\frac{2}{3}} + b_3\theta^{\frac{5}{3}} + b_4\theta^{\frac{16}{3}} + b_5\theta^{\frac{43}{3}} + b_6\theta^{\frac{110}{3}} \tag{10}$$

$$\ln\left[\frac{\rho_{g\,\text{sat}}(T)}{\rho_c}\right] = c_1\theta^{\frac{2}{6}} + c_2\theta^{\frac{4}{6}} + c_3\theta^{\frac{8}{6}} + c_4\theta^{\frac{18}{6}} + c_5\theta^{\frac{37}{6}} + c_6\theta^{\frac{71}{6}} \tag{11}$$

The volume fractions are determined by Eq. (2) and the definition of the mixture density:

$$\rho = \alpha_g\rho_{g\,\text{sat}}(T) + \alpha_l\rho_{l\,\text{sat}}(T) \tag{12}$$

Equations (8–12) represent a closed algebraic system that permits the solution of all thermodynamic variables for equilibrium states inside the saturation zone.

Table 1 Parameters of the saturation equations from Oldenbourg[15]

	Coefficient		
Index	a	b	c
1	−7.85823	1.99206	−2.02957
2	1.83991	1.10123	−2.68781
3	−11.7811	−0.512506	−5.38107
4	22.6705	−1.75263	−17.3151
5	−15.9393	−45.4485	−44.6384
6	1.77516	-6.75615×10^5	−64.3486

D. EOS Solution Procedure

When the mixture form of the conservation equations [Eq. (1)] are solved, all mixture variable are determined throughout the computational domain: ρ, $\boldsymbol{u}$, and e. The appropriate EOS is then used to determine all other thermodynamic variables. The solution procedure starts with an estimation of the local temperature. Using the estimated temperature, one determines the liquid and gas saturation densities by Eqs. (10) and (11), respectively. If the mixture density ρ (determined from the conservation equations) is higher than the liquid saturation density for this temperature, then the fluid is pure liquid and the pressure is calculated by Eq. (4), and the new temperature by Eq. (5). Two others cases are possible. First, the mixture density may be lower than the saturation gas density. Here, the pressure is determined by Eq. (6) and the new temperature by Eq. (7). Second, when the mixture density is between the liquid and gas saturation densities, the volume fractions are determined by Eqs. (12) and (2), the pressure by Eq. (8), and the new temperature by Eq. (9). If the new temperature is equal to the initial estimated temperature, then the thermodynamic state is uniquely determined. Otherwise, one uses the last temperature as an initial estimation and the process is iterated. This procedure quickly converges without difficulty.

E. Accuracy of the EOS

It is known that the Tait EOS is accurate[11] for high-pressure liquid states. However, in the present study, the fluid states can also exist at relatively low pressures, near the liquid-gas-phase transition zone. Thus, for completeness, it is necessary to examine the accuracy of the EOS in the vicinity of the vapor–liquid saturation region.

Figure 2 represents various isothermal curves for pure water in the (P, ρ) plane. The modified Tait EOS (shown as solid lines) is perfectly connected to the liquid saturation curve over a range of temperatures. Also shown on this graph are experimental data points. For temperatures lower than 560 K, the Tait EOS agrees well with the data over pressures ranging from saturation through 300 atm. For temperatures between 560 and 600 K, deviations between the data and EOS are noticeable. In fact, when approaching the critical point, nearly all EOSs present the same inaccuracies. Similarly, the isotherms computed from the ideal gas EOS are not well connected to the gas-saturation curve. As demonstrated in the following sections, the anticipated maximum temperature for all cases is less than 600 K.

Finally, it is clear that the isotherms inside the saturation region are straight lines. This means that supercritical states are not considered as previously mentioned by the equilibrium assumption. A consequence of this is that the second derivatives of the EOS are always positive, and the corresponding EOS is suitable for resolution with the Euler equations.

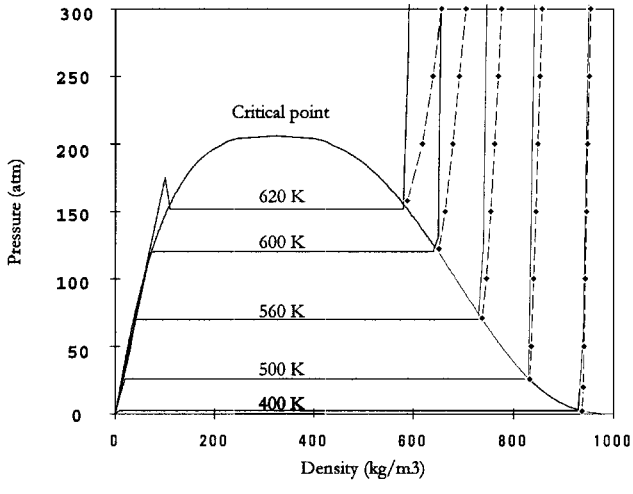

Fig. 2 Computed and experimental isotherms for water: ——, chosen equation of state; and – – – (with dots), represent experimental data.

IV. Numerical Solution

To accurately compute the various discontinuities present in the flow, the two-dimensional axisymmetric Euler equations [Eq. (1)] are written in conservative form:

$$\frac{\partial \boldsymbol{U}}{\partial t} + \frac{\partial \boldsymbol{F}}{\partial z} + \frac{\partial \boldsymbol{G}}{\partial r} + \boldsymbol{H} = 0 \tag{13}$$

with

$$\boldsymbol{U} = (\rho, \rho u, \rho v, \rho E)^T$$

$$\boldsymbol{F} = [\rho u, \rho u^2 + P, \rho uv, u(\rho E + P)]^T$$

$$\boldsymbol{G} = [\rho v, \rho uv, \rho v^2 + P, v(\rho E + P)]^T$$

$$\boldsymbol{H} = 1/r[\rho v, \rho uv, \rho v^2, v(\rho E + P)]^T$$

The conservative formulation is often used when dealing with aerodynamic applications. However, it can be shown that when dealing with flows where the total energy is dominated by kinetic energy, this formulation can result in very large errors in the internal energy calculation. As a consequence, the predicted temperature can be in error.[16–18] Accurate prediction of temperature is very important in hypervelocity cavitation because it determines the fluid phase (liquid, gas, two phase, or supercritical) and is used in the computation of pressure. It has been shown recently by Cocchi et al.[16] that when solving the Euler equations for pure gas flows with the ideal gas EOS, all conservative schemes (even high-resolution ones) fail when the total energy is mainly kinetic and the density tends to zero. The present hypervelocity cavitation problem is characterized by these same conditions. To illustrate the errors produced by applying conservative methods to the present problem, a simple one-dimensional test case is solved.

Consider a tube filled with a constant specific-heat perfect gas, initially at uniform pressure and density. Initially, the fluid occupying the right-half of the tube is set into motion to the right, and the fluid on the left-half of the tube is set into motion in the opposite direction. The initial conditions chosen for this example are $u_0 = 500$ m/s, $P_0 = 10^5$ Pa, and $\rho_0 = 1$ kg/m^3, and the ratio of specific heats γ is equal to 1.4. These conditions do not correspond to the creation of a strong vacuum, but do illustrate a case where a fairly large decrease in fluid temper ature is expected. The initial conditions are illustrated in Fig. 3. The exact solution of this test problem consists of two rarefaction waves, one propagating to the right and the other to the left. The exact solution can be obtained analytically. The results obtained with various conservative schemes are represented in Fig. 4. Compared are the Godunov-type methods with exact and approximate Riemann solvers (HLLE, Einfeld et al.[17]), high-order or low-order, and also centered methods, such as the MacCormack scheme.[19] All conservative methods fail to resolve the rarefaction waves accurately. One can notice a nonphysical entropy production (Fig. 4) and a strong temperature increase at the

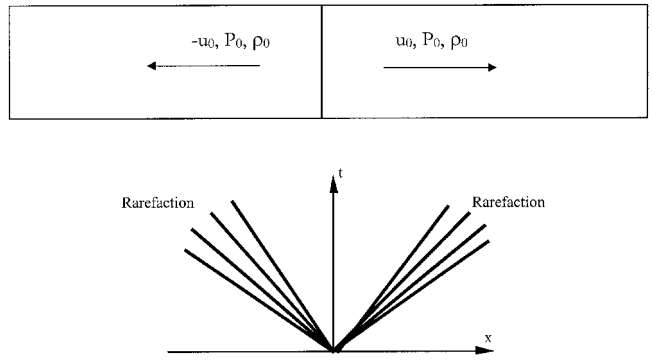

Fig. 3 Initial conditions and resulting characteristics for test problem consisting of opposing rarefaction waves.

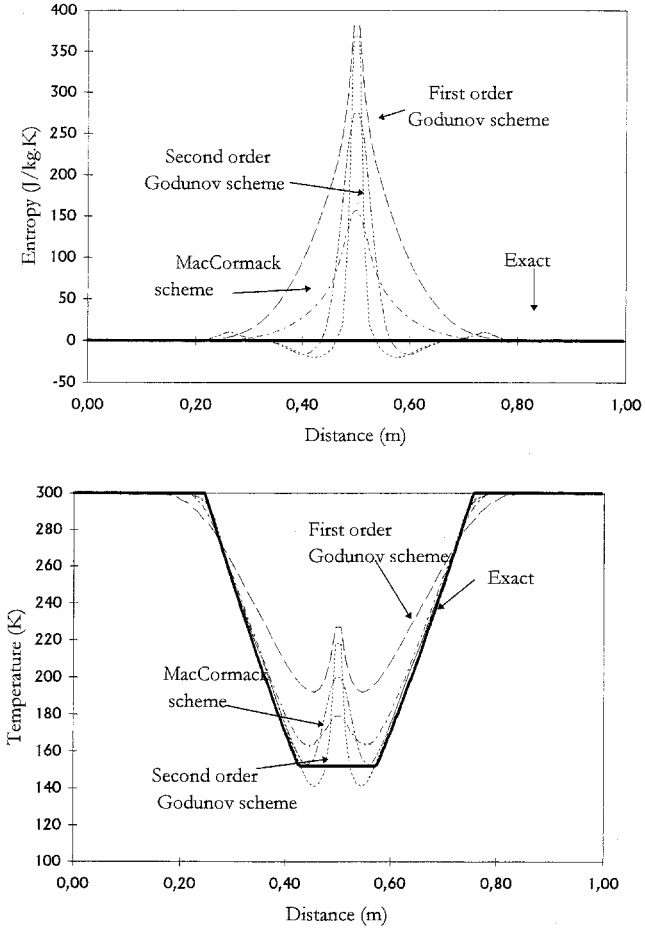

Fig. 4 Entropy and temperature profiles obtained with the conservative formulation and various numerical schemes for the test case illustrated in Fig. 3: ——, exact solution.

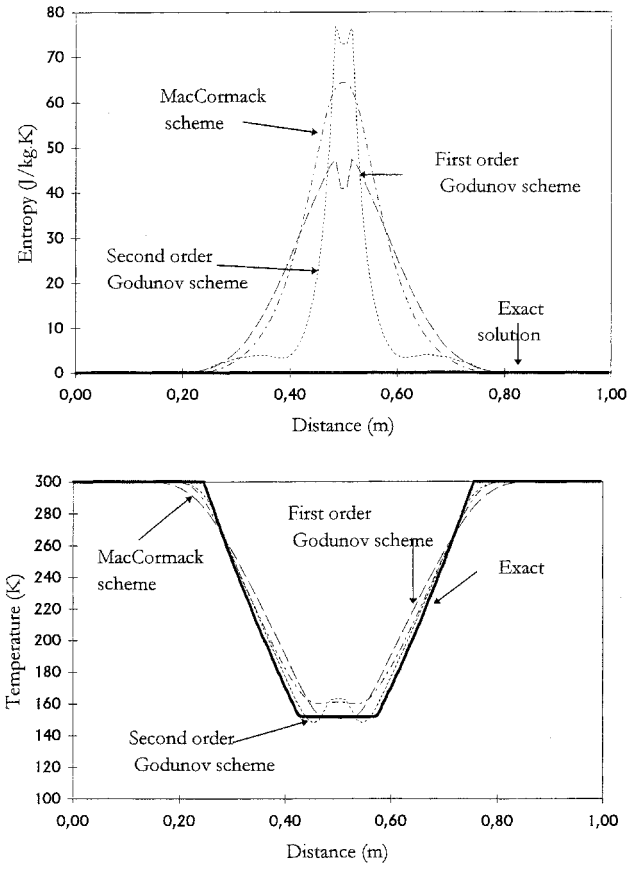

Fig. 5 Entropy and temperature profiles obtained with the nonconservative formulation and various numerical schemes for the test case illustrated in Fig. 3: ——, exact solution.

center of the physical domain (Fig. 5). These artifacts are not acceptable for the present application where phase change is expected to occur. Indeed, the erroneous temperature increase in the context of the cavitation problem is likely to produce artificial thermodynamic conditions corresponding to a supercritical fluid. These errors are a result of an erroneous estimate of the velocity, resulting in an error in the kinetic energy. These errors propagate to the internal energy and temperature because they are obtained by the combination of total and kinetic energies. One way to overcome this problems is to solve the energy equation in terms of internal energy instead of total energy. This procedure is not conservative, but it has been shown that strict conservativity is not required to obtain accurate solutions.[20] But, of course, conservativity must be maintained as much as possible. In one dimension, the internal energy equation is written as

$$\frac{\partial \rho e}{\partial t} + \frac{\partial \rho e u}{\partial x} = -P\frac{\partial u}{\partial x} \tag{14}$$

Equation (14) is solved in conjunction with the mass and momentum equations and forms a nonconservative system. When this system of equations is solved for the problem illustrated in Fig. 3, the results are acceptable and major errors in the temperature predictions have been reduced (Fig. 5).

The nonconservative system cannot be used for the solution in all configurations. In particular, it cannot be used for capturing shock waves. To overcome this difficulty a hybrid formulation of the equations has been developed. There is no need to change the formulation of the mass and momentum equations for the hybrid solution. However, for capturing shock waves, the energy equation must be written in conservative form [Eq. (13)]. Other flow regimes are more favorably handled, in particular rarefaction waves, if the energy equation is written in terms of internal energy. In one dimension, the energy equation is then replaced by a mixed formulation [Eq. (15)]:

$$\frac{\partial \rho e + \beta(0.5\rho u^2)}{\partial t} + \frac{\partial \rho e u + \beta(0.5\rho u^2 + P)u}{\partial x} = -(1-\beta)P\frac{\partial u}{\partial x} \tag{15}$$

where β is a shock wave sensor: $\beta = 1$ at shock waves and $\beta = 0$ otherwise.

Here, the artificial viscosity of Richtmyer and Morton[21] is used for the one-dimensional calculations as a shock indicator. It is defined by

$$\text{If} \quad \Delta = u_{i+1} - u_{i-1} \geq 0 \quad \text{then} \quad S_{\text{shock}} = (\rho/P)\Delta^2$$

$$\text{else} \quad S_{\text{shock}} = 0$$

If $S_{\text{shock}} > 0.01$, then we employ the conservative formulation by imposing $\beta = 1$ in Eq. (15).

Here, a modification of the MacCormack scheme is used to numerically resolve the equations. As demonstrated previously, it is possible to build an accurate method on the basis of the hybrid system, e.g., a Godunov-type scheme. However, these methods need an exact (or approximate) Riemann solver. In the context of the hypervelocity cavitation problem with a complicated EOS, it is not reasonable to use such methods. For the present application, a centered scheme, e.g., MacCormack, is preferred. This method does not require a Riemann solver.

The system of conservation laws is written in a two-dimensional hybrid formulation. In integral form, it is written as

$$\frac{\partial}{\partial t}\int_{\Omega} U \, d\Omega + \int_{s} \boldsymbol{F}\cdot d\boldsymbol{S} + \int_{s} B(\boldsymbol{V}\cdot d\boldsymbol{S}) + \int_{\Omega} \boldsymbol{H} = 0 \tag{16}$$

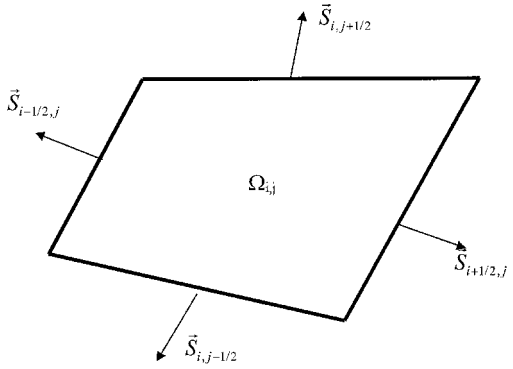

Fig. 6 Control volume and normal vectors used in formulation.

with

$$U = \left[\rho, \rho u, \rho v, \rho e, \tfrac{1}{2}\beta\rho(u^2+v^2)\right]^T, \qquad \boldsymbol{F} = (f, g)^T$$

$$f = \left(\rho u, \rho u^2 + P, \rho u v, u\left\{\rho e + \beta\left[P + \tfrac{1}{2}\rho(u^2+v^2)\right]\right\}\right)^T$$

$$g = \left(\rho v, \rho u v, \rho v^2 + P, v\left\{\rho e + \beta\left[P + \tfrac{1}{2}\rho(u^2+v^2)\right]\right\}\right)^T$$

$$B = [0, 0, 0, (1-\beta)P]^T, \qquad \boldsymbol{V} = (u, v)^T$$

$$\boldsymbol{H} = 1/r[\rho v, \rho u v, \rho v^2, v(\rho E + P)]^T$$

Equation (16) applied to the control volume of Fig. 6 is written as

$$\frac{\partial(\boldsymbol{U}_{i,j}\Omega_{i,j})}{\partial t} + \sum_{\text{sides}} \boldsymbol{F}\cdot\boldsymbol{S} + B_{i,j}\sum_{\text{sides}} \boldsymbol{V}\cdot\boldsymbol{S} + \boldsymbol{H}_{i,j}\Omega_{i,j} = 0 \quad (17)$$

Equation (17) is solved by the second-order-accurate MacCormack scheme on a quadrilateral composed mesh. Equation (17) is discretized in two steps. The predictor step writes:

$$\tilde{\boldsymbol{U}}_{i,j} = \boldsymbol{U}^n_{i,j} - (\Delta t/\Omega_{i,j})[\Phi_p(\boldsymbol{F}_{i,j}) + B_{i,j}\Phi_p(\boldsymbol{V}_{i,j})] - \Delta t\boldsymbol{H}_{i,j} \quad (18)$$

where for a vector $\boldsymbol{A}_{i,j}$, the function Φ_p is expressed by

$$\Phi_p(\boldsymbol{A}_{i,j}) = \boldsymbol{A}^n_{i+1,j}\cdot\boldsymbol{S}_{i+\frac{1}{2},j} + \boldsymbol{A}^n_{i,j+1}\cdot\boldsymbol{S}_{i,j+\frac{1}{2}} + \boldsymbol{A}^n_{i,j}\cdot\boldsymbol{S}_{i-\frac{1}{2},j} + \boldsymbol{A}^n_{i+1,j}\cdot\boldsymbol{S}_{i,j-\frac{1}{2}}$$

The corrector step is defined by

$$\bar{\tilde{\boldsymbol{U}}}_{i,j} = \boldsymbol{U}^n_{i,j} - (\Delta t/\Omega_{i,j})[\Phi_c(\bar{\tilde{\boldsymbol{F}}}_{i,j}) + B_{i,j}\Phi_c(\bar{\tilde{\boldsymbol{V}}}_{i,j})] - \Delta t\bar{\tilde{\boldsymbol{H}}}_{i,j} \quad (19)$$

where for a vector $\boldsymbol{A}_{i,j}$, the function Φ_c is expressed by

$$\Phi_c(\bar{A}_{i,j}) = \bar{\boldsymbol{A}}^n_{i,j}\cdot\boldsymbol{S}_{i+\frac{1}{2},j} + \bar{\boldsymbol{A}}_{i,j}\cdot\boldsymbol{S}_{i,j+\frac{1}{2}} + \bar{\boldsymbol{A}}^n_{i-1,j}\cdot\boldsymbol{S}_{i-\frac{1}{2},j} + \bar{\boldsymbol{A}}^n_{i,j-1}\cdot\boldsymbol{S}_{i,j-\frac{1}{2}}$$

The final expression of vector $\boldsymbol{U}$ at time t_{n+1} is obtained by

$$\boldsymbol{U}^{n+1}_{i,j} = \tfrac{1}{2}(\tilde{\boldsymbol{U}}_{i,j} + \bar{\tilde{\boldsymbol{U}}}_{i,j}) \quad (20)$$

followed by a standard second-order artificial viscosity step:

$$\tilde{\boldsymbol{U}}^{n+1}_{i,j} = \boldsymbol{U}^{n+1}_{i,j} + \eta\left(\boldsymbol{U}^{n+1}_{i+1,j} - 2\boldsymbol{U}^{n+1}_{i,j} + \boldsymbol{U}^{n+1}_{i-1,j} + \boldsymbol{U}^{n+1}_{i,j+1} - 2\boldsymbol{U}^{n+1}_{i,j} + \boldsymbol{U}^{n+1}_{i,j-1}\right)$$

The artificial viscosity coefficient η has been determined by numerical tests to be as small as possible and to preserve oscillation-free solutions. For the meshes we have used, and under the stiff conditions of our problems, a typical value for η is 10^{-2}.

The time step Δt is chosen to fulfill the Courant–Friedrichs–Lewy (CFL) criterion. In the computations we have used the following definition:

$$\Delta t = \text{CFL} \times \min_{(i,j)} \times \left(\frac{\Omega_{i,j}}{\left|\boldsymbol{V}_{i,j}\cdot\boldsymbol{S}_{ih-\frac{1}{2},j}\right| + \left|\boldsymbol{V}_{i,j}\cdot\boldsymbol{S}_{i,j-\frac{1}{2}}\right| + c_0\sqrt{\left|\boldsymbol{S}_{i+\frac{1}{2},j}\right|^2 + \left|\boldsymbol{S}_{i,j+\frac{1}{2}}\right|^2}}\right)$$

where c_0 is the liquid sound speed under atmospheric conditions, and CFL has been chosen equal to 0.3.

At the beginning of each time step, the value of the shock wave sensor β is computed. At each mesh point, the two different forms of the energy flux are computed. Indeed, a mesh point where $\beta = 0$ may be a neighbor with a point where $\beta = 1$. The flux differences must always be performed with the same fluxes: conservative or nonconservative. Therefore, the two fluxes are necessary at all mesh points. This modified MacCormack scheme is now used with the cavitation model for several one- and two-dimensional test cases.

V. Results

A. One-Dimensional Cavitation Tube

To test the numerical accuracy of the proposed model, a one-dimensional test case similar to the previous test case (Fig. 3) is modeled. This example corresponds to a tube of arbitrary length, initially filled with liquid water at atmospheric conditions. The fluid in the left chamber has an initial velocity of −3000 m/s, whereas the fluid in the right chamber is moving at the same velocity in the opposite direction. The solution to this test case corresponds to two rarefaction waves running in opposite directions, resulting in vaporization of the liquid in the central region.

Results of various properties are shown at 30, 60, 90, and 120 μs in Fig. 7. Figure 7a shows the velocity profiles. The fluid velocity decreases across the rarefaction waves reaching zero velocity at the center of the domain. These strong rarefaction waves (right and left running) induce a strong decrease in density from the initial value of 1000 kg/m^3 to pure vapor values~3 orders of magnitude less dense (Fig. 7b). Similarly, the pressure represented in Fig. 7c decreases across the rarefaction waves and reaches the saturation pressure at the corresponding temperature. Vapor is being produced at a constant temperature because of the assumption of local equilibrium during phase change. When the fluid becomes a pure gas, the rarefaction effects continue, and the gas temperature again decreases (Fig. 7d). These effects are clearly visible on the pressure profiles (Fig. 7c). The pressure decreases abruptly in the pure liquid, then reaches the saturation pressure and remains constant. It then decreases again in the pure gas phase near the center of the domain. One can also notice that the temperature at the center of the domain does not demonstrate an unphysical increase in the gas region, a feature observed when the conservative form of the equations are solved (Fig. 4). Here, the hybrid formulation allows the computation of physically reasonable results. For the initial conditions studied, the two rarefaction waves are sufficiently strong to evaporate all of the liquid. Across these waves, the gas volume fraction starts at $\alpha_g = 0$ and reaches $\alpha_g = 1$ progressively (Fig. 7e).

The rarefaction-driven vaporization observed in this one-dimensional test case is representative of what will occur in the wake of the two-dimensional hypersonic projectile. Before proceeding to the two-dimensional computation, the model and the solution method will be tested with an additional one-dimensional test case corresponding to shock-driven condensation.

B. One-Dimensional Shock-Condensation Tube

We now consider a shock-tube test case where the fluid exhibits phase transition. Here, a 1-m-length tube is filled on the left-half with a high-pressure liquid (water) at the initial density of 1200 kg/m^3, and on the right-half with a two-phase (liquid/vapor) mixture at an initial density of 500 kg/m^3. Initially, the two fluids have a common temperature of 300 K. The two-phase mixture is composed of 50% liquid and 50% vapor on a mass basis.

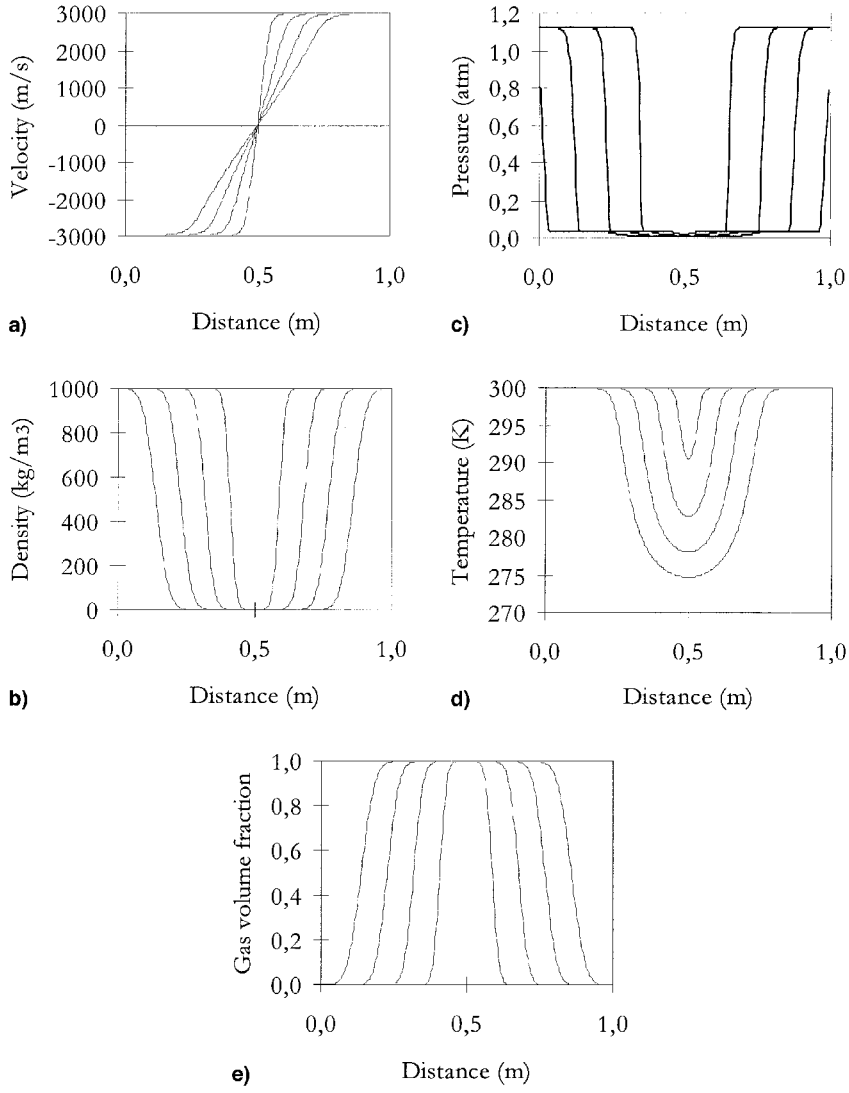

Fig. 7 Flow variable profiles for the one-dimensional cavitation test problem (Fig. 3) at 30, 60, 90, and 120 μs.

Figure 8 shows the various property profiles at 75, 150, 225, 300, and 375 μs to illustrate the wave propagation. Initially, the high-pressure chamber communicates with the low-pressure side, and a strong rarefaction wave facing to the left propagates into the liquid while a shock wave propagates into the two-phase mixture on the right (Fig. 8a). Across the shock wave, the density increases from the ambient 500 kg/m^3 to a shock-compressed 1040 kg/m^3. Consequently, the vapor contained in the two-phase mixture condenses instantaneously across the shock wave. The plateau of density of the shocked mixture and expanded liquid are the same. In the numerical solution procedure used in this study, the Tait EOS is activated when the local fluid state reaches pure liquid density values. This EOS generates only two characteristic directions for the wave propagation ($u \pm c$) with our flow model. Indeed, it is uncoupled from the temperature, and the expected contact surface is not present on the density profiles.

The shock-wave indicator β is represented in Fig. 8b. This parameter tracks the shock-wave's position. Its value is equal to unity for meshes corresponding to the shock-wave capturing. The conservative formulation of Eq. (15) is used only for these mesh points; i.e., $\beta = 1$. Elsewhere in the solution domain, the nonconservative formulation of Eq. (15) is used ($\beta = 0$).

Figure 8c shows the vapor volume fraction. It shows that the vapor in the two-phase mixture is condensed immediately behind the shock wave. The gas-volume fraction starts from $\alpha_g = 0.5$ and reaches $\alpha_g = 0$ across this wave. The condensation phenomena is instantaneous in the model because it assumes local thermodynamic equilibrium. In reality, there is a finite time required to achieve equilibrium, which has the effect of smearing out the discontinous profiles. Thus, the shock wave adjusts its intensity regarding all hydrodynamic and phase-change processes and there is no relaxation process behind the shock wave. This is shown on the velocity and pressure profiles of Figs. 8d and 8e.

The temperature profiles are represented in Fig. 8f. The fluid increases in temperature across the shock wave and decreases across the rarefaction waves. A contact surface is clearly visible between these two regions. One can also notice that the wave propagation is very different in the pure liquid and the two-phase mixture.

This shock-driven condensation test case puts in evidence the various phenomena occurring in such a flow, and demonstrates that the model can predict condensation as well as cavitation. The results predicted by the model are consistent with the expected results.

C. Two-Dimensional Hypervelocity Projectile Simulations

The following two-dimensional, unsteady calculations initiate with water (100% liquid) at atmospheric pressure and temperature flowing over a projectile with a finite velocity imposed at the inflow boundary. For all two-dimensional simulations presented here, the boundary conditions are the same. The projectile surface is treated as a rigid wall with centerline symmetry. The outflow and upstream boundaries are treated as nonreflecting boundaries. At the inflow boundary on the left-hand side, the fluid is pure liquid and moving at 3000 m/s (supersonic relative to the liquid sound speed). The

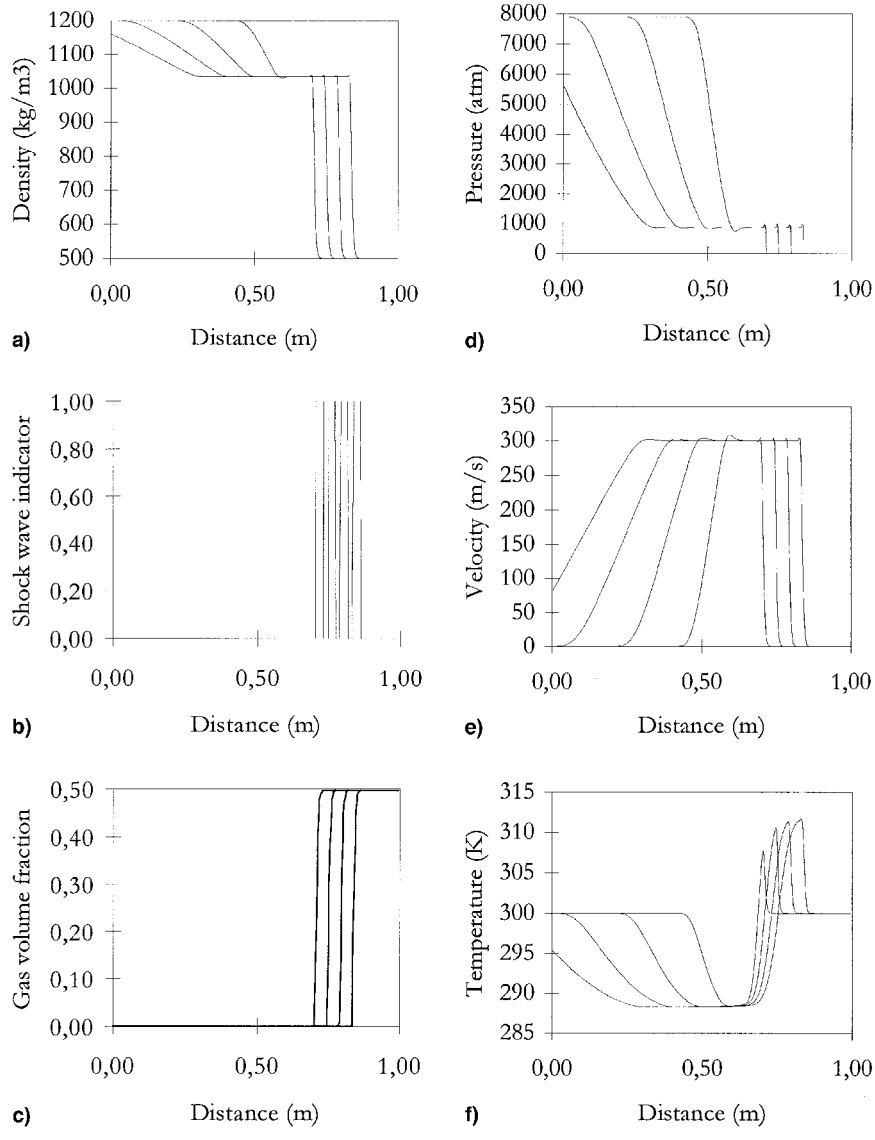

Fig. 8 Flow variable profiles for a one-dimensional shock condensation test problem at 75, 150, 225, and 300 μs.

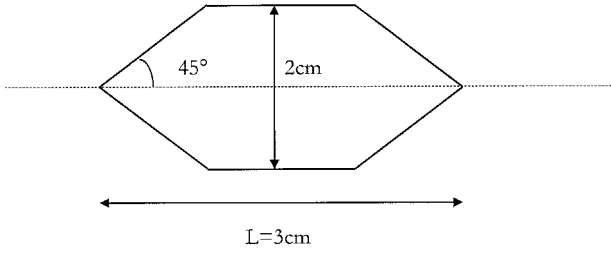

Fig. 9 Shape and dimensions of the two-dimensional hypersonic projectile.

projectile has dimensions shown in Fig. 9. Because the inflow is supersonic, a detached shock wave is expected in front of the obstacle, as represented in Fig. 1. On the two angular points connecting the cones to the cylindrical portion, strong rarefaction waves are expected, possibly capable of inducing cavitation.

Density contours are presented in Fig. 10 at 75 μs increments to illustrate the unsteady shock wave and formation of a cavitation pocket. This is the most representative flow variable for the hypersonic projectile case. Initially, the computational domain contains pure liquid. Cavitation begins between the two trailing-edge angular points and forms a pocket impinging on the symmetry axis. The predictions show the cavitation pocket is stable. The final time represents a steady gas pocket that exits the computational domain. The large scale of the density variations (0–1350 kg/m^3) required to illustrate the cavitation pocket makes it difficult to represent details of the flow internal to the wake. However, it is possible to show a magnified view of the steady-state density contours internal to the wake. Figure 11 shows density contours ranging between 0 and 70 kg/m^3 to help illustrate the recompression shock that appears in the flow when the fluid trajectories impinges the symmetry axis. This shock wave does not have a major influence on the fluid density variations of the cavitation pocket.

The gas-volume fraction is a choice variable for visualizing the cavitation zone. Figure 12a shows the gas-volume fraction corresponding to the last instant (375 μs) shown in Fig. 10, i.e., steady-state condition. Here, cavitation begins at the first angular point connecting the nose to the cylindrical portion of the obstacle, and complete vaporization is reached when the flow expands at the trailing-edge angular point. Maximum gas-volume fraction is obtained in the wake of the projectile and corresponds to ~98% gas. Figure 12b represents a plot of the corresponding gas-volume fraction measured along the projectile surface. Note that a pure gas zone is not achieved because of numerical diffusion of the density discontinuity. It is well known that density discontinuity is the most difficult discontinuity to handle in compressible flows. Along a radius normal to the centerline, the density profile evolves as shown in Fig. 13. Numerical diffusion induces a smoothed contact discontinuity. To

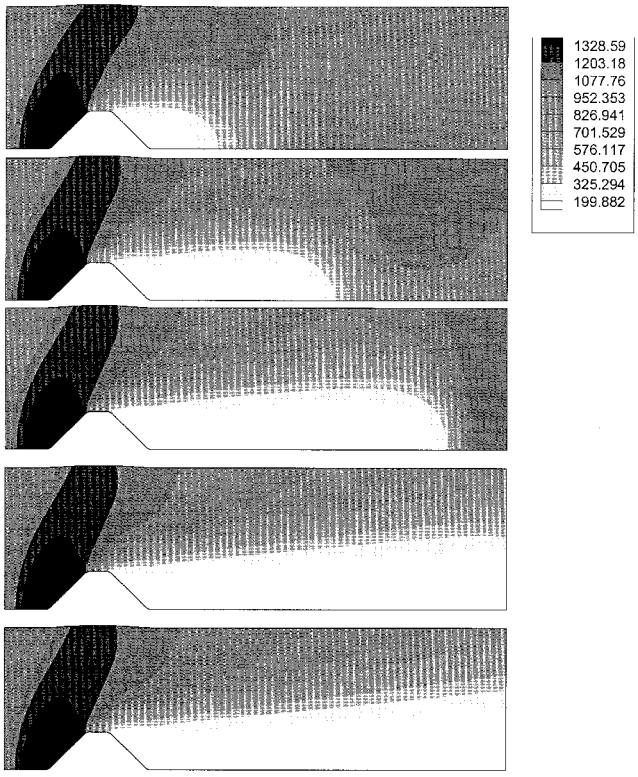

Fig. 10 Density contours (kg/m^3) at 75, 150, 225, 300, and 375 μs (top to bottom) showing the unsteady evolution of the shock wave and cavitation pocket for the two-dimensional projectile shown in Fig. 9.

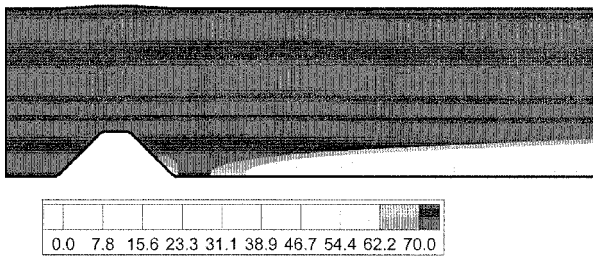

Fig. 11 Magnified view of the density contours (kg/m^3) corresponding to t = 375 μs in Fig. 10.

reduce the effect of numerical diffusion, we have used a mesh composed of 152 cells along the longitudinal direction and 45 radial cells. With a coarser mesh, the maximum gas-volume fraction decreases, indicating that numerical diffusion is responsible for this defect.

Figure 14 represents the temperature contours. Similar to the density contours, the temperature increases at the shock wave, then this fluid is convected along the projectile and decreases in temperature across rarefaction waves. One can notice that the temperature levels are always moderated and never correspond to supercritical fluid. Thus, the EOS is only being applied to fluid states where it shows high accuracy.

D. Parametric Study

A study was performed on the influence of inflow velocity and of the angle of attack of the projectile on the size of the cavitation pocket. For comparison purposes, the height of the cavitation pocket is computed at the axial distance of 4L (L is defined in Fig. 9) in the wake of the projectile. For all cases studied, the height and length of the projectile are held constant. The boundary of the envelope is defined as the radial location where the gas-volume fraction reaches the value of 0.3. Results are summarized in Fig. 15.

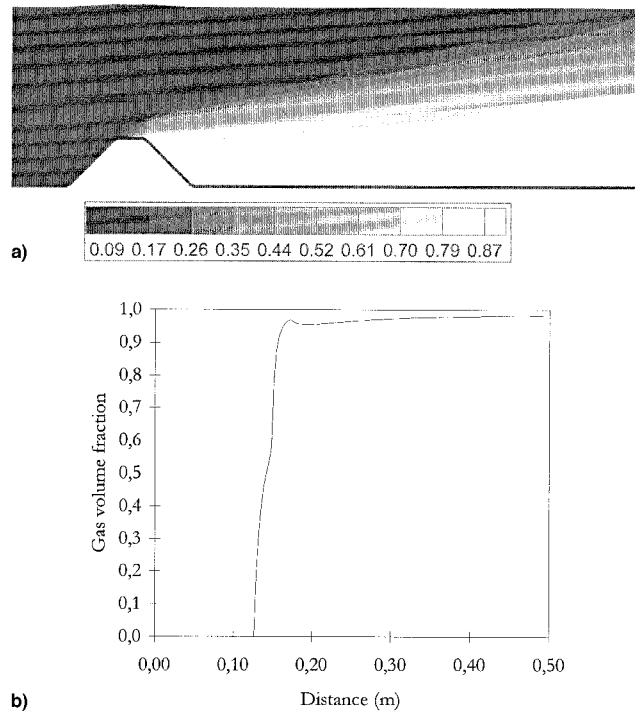

Fig. 12 Gas-volume fractions at time frame t = 375 μs in Fig. 10: a) contours and b) profile measured along the projectile axis.

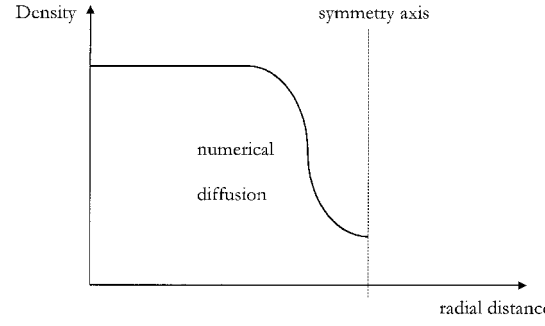

Fig. 13 Illustration of numerical diffusion in density profile along axis normal to centerline.

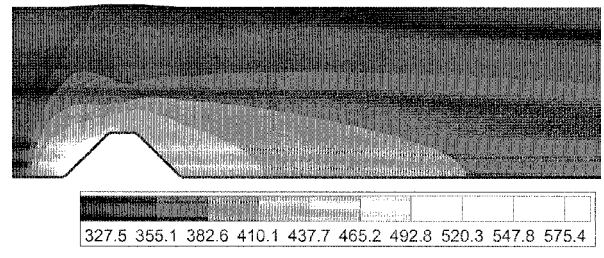

Fig. 14 Temperature contours (K) at t = 375 μs time frame shown in Fig. 10.

The nose of the projectile is a ramp behind which a cavitation pocket develops. For a given inflow Mach number, the dimensionless pocket height Y/L increases when the cone angle also increases. Also, for a given angle, the pocket size increases when inflow velocity increases. But when the attack angle reaches 45 deg, the pocket height no longer depends on the attack angle and inflow velocity. For the high-velocity flows we are studying here, the ramp effect is eliminated for an attack angle larger than 45 deg.

We now investigate the influence of the height H of the projectile (the radius of the cylindrical portion) on the height of the cavitation

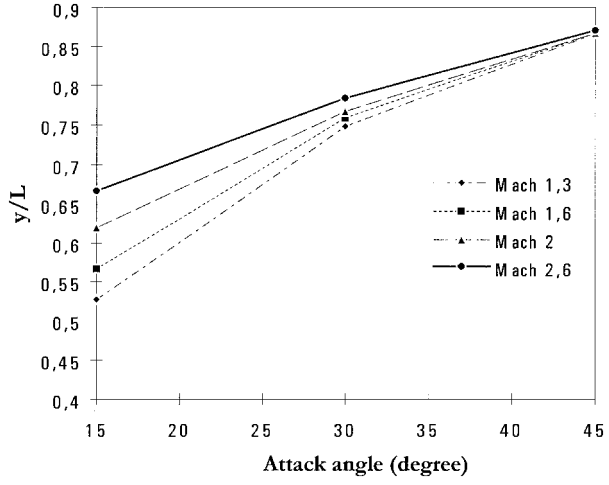

Fig. 15 Variation of the steady-state dimensionless pocket height *Y/L* at various inflow Mach numbers.

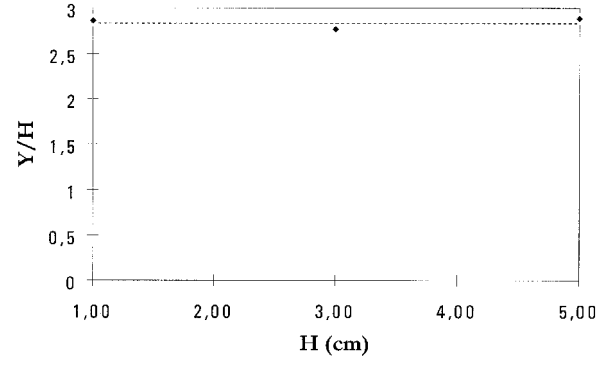

Fig. 16 Variation of the steady-state dimensionless pocket height *Y/H* as a function of projectile height *H*.

pocket (Y/H). Results are represented in Fig. 16. This figure shows that the dimensionless heights of the cavitation pocket at $4L$ in the wake of the projectile do not depend on the height of it. These calculations have been performed for an inflow Mach number of 2 and a constant attack angle of 30 deg.

VI. Conclusions

A model for cavitation at high velocity has been developed. It takes into account liquid, gas, and mixture compressibility effects. It is based on the construction of an EOS, that connects the compressible Tait EOS for the pure liquid, and the ideal gas law for pure vapor, to the saturation curve. The mixture properties are deduced from the phase diagram of water, under the assumption of thermodynamic equilibrium and for thermodynamic states below the critical point.

The flow model is cast in a manner similar to the Euler equations. It has been shown that their solution is difficult for high-velocity flows when dealing with cavitation applications, even with pure gas. The solution proposed herein is a modification of the MacCormack scheme.

The model is tested on one-dimensional applications and shows a reasonable agreement with phenomena that are expected. It is then applied to the two-dimensional case for the computation of the cavitation effects in the wake of a hypervelocity projectile. Again, results show a reasonable agreement. Following this a parametric study is developed about the geometrical parameters and the inflow Mach number on the size of the cavitation pocket.

Acknowledgments

Part of this study was supported by Direction generale de l'Armement, Centre Technique des Systemes Naval, Toulon. Robert Tosello is gratefully acknowledged.

References

[1]Lemonnier, H., and Rowe, A., "Another Approach in Modeling Cavitating Flows," *Journal of Fluid Mechanics*, Vol. 195, 1988, pp. 557–580.

[2]Kubota, A., Kato, H., and Yamaguchi, H., "A New Modeling of Cavitating Flows: A Numerical Study of Unsteady Cavitation on a Hydrofoil Section," *Journal of Fluid Mechanics*, Vol. 240, 1992, pp. 59–96.

[3]Kinnas, S. A., and Fine, N. F., "A Numerical Nonlinear Analysis of the Flow Around Two- and Three-Dimensional Partially Cavitating Hydrofoils," *Journal of Fluid Mechanics*, Vol. 254, 1993, pp. 151–181.

[4]Davies, G. A., Flanagan, O., Hillier, R., Hitchings, D., and Lord, S. J., "Hydraulic Shock Loading Due to Supercavitating Projectiles," *Proceedings of the 20th International Symposium on Shock Waves*, edited by B. Sturtevant, J. E. Sheperd, and H. G. Hornuns, Vol. 2, World Scientific, NJ, 1995, pp. 1207–1212.

[5]Thibaudier, C., and Tosello, R., "Interaction Jets de Charge Creuses—Eau" *Actes du 4eme Symposium International des Hautes Pressions Dynamiques*, edited by AFP La Ferte, Saint Aubin, France, 1995, pp. 281–287.

[6]Arcoumanis, C., Gavaises, M., and French, B, "Effect of Fuel Injection Processes on the Structure of Diesel Sprays," *SAE Transactions*, Vol. 106, No. 3, 1997, pp. 1025–1064.

[7]Butler, P. B., Lambeck, M. F., and Krier, H., "Modeling of Shock Development and Transition to Detonation Initiated by Burning in Porous Propellant Beds," *Combustion and Flame*, Vol. 46, 1982, pp. 75–93.

[8]Saurel, R., Larini, M., and Loraud, J. C., "Ignition and Growth of a Detonation by a High Energy Plasma," *Shock Waves*, Vol. 2, No. 1, 1992, pp. 91–102.

[9]Rogue, X., Rodriguez, G., Haas, J. F., and Saurel, R., "Experimental and Numerical Investigation of the Shock-Induced Fluidization of a Particle Bed," *Shock Waves*, Vol. 8, No. 1, 1998, pp. 29–45.

[10]Reid, C. R., Prausnitz, M. J., and Poling, E. B., *The Properties of Gases and Liquid*, 4th ed., McGraw–Hill, New York, 1987.

[11]Saul, A., and Wagner, W., "A Fundamental Equation for Water Covering the Range from the Melting Line to 1273 K at Pressure up to 2500 MPa," *Journal of Chemical Physics*, Vol. 18, 1989, pp. 1537–1564.

[12]Godunov, S. K., Zabrodine, A., Ivanov, M., Kraiko, A., and Prokopov, G., *Resolution Numerique des Problèmes Multidimensionnels de la Dynamique des Gaz*, Mir, Moscow, 1979.

[13]Toro, E. F., *Riemann Solvers and Upwind Methods for Fluid Dynamics*, Springer–Verlag, Berlin, 1997.

[14]Cole, R. H., *Underwater Explosions*, Princeton Univ. Press, Princeton, NJ, 1948.

[15]Oldenbourg, R., *Properties of Water and Steam in SI-Units*, Springer–Verlag, Berlin, 1989.

[16]Cocchi, J. P., Saurel, R., and Loraud, J. C., "Some Remarks About the Resolution of High Velocity Flows near Low Densities," *Shock Waves*, Vol. 8, No. 2, 1998, pp. 119–125.

[17]Einfeld, B., Munz, C. D., Roe, P. L., and Sjögreen, B., "On Godunov-Type Methods near Low Densities," *Journal of Computational Physics*, Vol. 92, 1991, pp. 273–295.

[18]Toro, E. F., "Some IVPs for Which Conservative Methods Fail Miserably," *Proceedings of the 6th International Symposium on Computational Fluid Dynamics*, edited by E. Hafez, Vol. 3, 1995, pp. 1294–1299.

[19]MacCormack, R. W., "The Effect of Viscosity in Hypervelocity Impact Cratering," AIAA Paper 69-354, Aug. 1969.

[20]Karni, S., "Hybrid Multifluid Algorithms," *SIAM Journal of Scientific Computing*, Vol. 17, No. 5, 1996, pp. 1019–1039.

[21]Richtmyer, R. D., and Morton, K. W., *Difference Methods for Initial-Value Problems*, Wiley, New York, 1967.